



Article

# Microheater Topology for Advanced Gas Sensor Applications with Carbyne-Enriched Nanomaterials

Mariya Aleksandrova <sup>1,\*</sup>, Belgina Ustova <sup>1</sup>, Tsvetozar Tsanev <sup>1</sup>, Ioannis Raptis <sup>2</sup>, Angeliki Tserepi <sup>2</sup>, Evangelos Gogolides <sup>2</sup> and Georgi Kolev <sup>1</sup>

<sup>1</sup> Department of Microelectronics, Technical University of Sofia, 1756 Sofia, Bulgaria; belginaustova@gmail.com (B.U.); zartsanev@tu-sofia.bg (T.T.); georgi\_klv@abv.bg (G.K.)

<sup>2</sup> NCSR Demokritos, 15341 Athens, Greece; i.raptis@inn.demokritos.gr (I.R.); a.tserepi@inn.demokritos.gr (A.T.); e.gogolides@inn.demokritos.gr (E.G.)

\* Correspondence: m\_aleksandrova@tu-sofia.bg; Tel.: +359-2-965-30-85

**Featured Application:** Biomedical or environmental monitoring sensors.

**Abstract:** The response characteristics of carbyne-enriched surface-acoustic-wave (SAW)-based gas sensors utilizing meander and rectangular microheater topologies were investigated to assess their desorption and recovery properties. Comparative analysis of contact resistance and interface capacitance before and after heating revealed minimal deviation in contact resistance, signifying strong thermal stability in the carbyne-enriched layer. However, the interface capacitance varied with the microheater size. Our analysis reveals that a small meander microheater configuration (line width: 300  $\mu\text{m}$ ) facilitates efficient sensor recovery at ethanol concentration measurements in the range of 180–680 ppm, maintaining a low deviation in time delay across different concentrations (~2.3%), resulting in a narrow hysteresis and linear sensor response. Conversely, the large meander microheater (line width: 450  $\mu\text{m}$ ) and rectangular dense microheater induce irreversible changes in the sensing structure, leading to a widened hysteresis at higher concentrations and increased power consumption. Recovery patterns display substantial deviations from initial values at different concentration levels. Higher concentrations exhibit broader hysteresis, while lower concentrations show narrower hysteresis loops, compared to the small meander microheater. The study offers insights into desorption rates, power consumption variations, and recovery behaviors related to different microheater configurations. It demonstrates the importance of microheater topology selection in tailoring recovery properties and response characteristics, contributing to the advancement of carbyne-based sensor technology.

**Keywords:** carbyne-enriched layer; SAW sensor; microheater topology; sensor recovery



**Citation:** Aleksandrova, M.; Ustova, B.; Tsanev, T.; Raptis, I.; Tserepi, A.; Gogolides, E.; Kolev, G. Microheater Topology for Advanced Gas Sensor Applications with Carbyne-Enriched Nanomaterials. *Appl. Sci.* **2024**, *14*, 1728. <https://doi.org/10.3390/app14051728>

Academic Editor: Nicola Pio Belfiore

Received: 30 January 2024

Revised: 9 February 2024

Accepted: 19 February 2024

Published: 21 February 2024



**Copyright:** © 2024 by the authors. Licensee MDPI, Basel, Switzerland. This article is an open access article distributed under the terms and conditions of the Creative Commons Attribution (CC BY) license (<https://creativecommons.org/licenses/by/4.0/>).

## 1. Introduction

Gas sensing technology is integral to a wide range of industrial, environmental, and healthcare applications, with a growing demand for high-performance sensors capable of detecting and quantifying trace amounts of specific gases. In industrial settings, gas sensors are essential for monitoring air quality, detecting leakages of hazardous gases, and ensuring workplace safety. For example, they are used in manufacturing facilities, chemical plants, and refineries to detect and mitigate the release of toxic or flammable gases, thereby safeguarding the wellbeing of workers and preventing potential accidents [1,2]. Within the environmental monitoring sector, gas sensors are deployed to assess and manage air pollution levels, detect harmful emissions from vehicles and industrial processes, and monitor indoor air quality in buildings. These sensors contribute to efforts aimed at protecting the environment and public health, and ensure compliance with air quality regulations and standards [3–5].

In the realm of healthcare, gas sensors are utilized in medical devices and monitoring systems to measure physiological gases, such as oxygen and carbon dioxide, in patients' breath and blood. They also find applications in diagnostic equipment for detecting volatile organic compounds and gases associated with various medical conditions, thereby aiding in disease diagnosis and management [6–8].

In recent years, surface acoustic wave (SAW) gas sensors have emerged as a promising technology for detecting and analyzing trace amounts of various gases [9–11]. Incorporating microheaters and advanced gas sensitive layers, such as carbyne, can greatly enhance these sensors' performance. Carbyne, as a gas-sensitive layer, offers unique properties that can significantly enhance sensor performance [12]. Carbyne, a one-dimensional carbon allotrope, exhibits exceptional sensitivity to organic vapors due to its high surface area, molecular reactivity, and potential for gas molecule adsorption. Carbyne can provide high selectivity and sensitivity when employed as the gas-sensitive layer in sensors. Its stability and responsiveness to changes in gas concentrations make it an ideal material for gas sensing applications. To ensure the reversibility of the response characteristics, the carbyne gas sensors, like most gas sensors, must be equipped with a microheater. This miniature heating element is strategically integrated into gas sensors to control the temperature of the gas-sensitive layer precisely. By applying controlled heating, microheaters facilitate the desorption of gas molecules from the gas-sensitive layer, thereby enhancing the sensor's responsiveness and recovery characteristics. Additionally, microheaters enable the modulation of the sensor temperature, which can influence the adsorption and desorption kinetics of gas molecules on the surface of the gas-sensitive layer, ultimately affecting the sensor's sensitivity, selectivity, and response time. As seen from the literature, the topologies of microheaters in gas sensors can vary based on the specific design requirements and performance objectives of the sensor. Some typical topologies include serpentine microheaters, interdigitated microheaters, dual-element microheaters, spiral-shaped microheaters, and others [13]. Each of these microheater topologies offers distinct advantages in terms of heat distribution, temperature control, and desorption kinetics, influencing the overall effectiveness of the gas sensor. The selection of a specific microheater topology is driven by considerations such as the targeted gas detection requirements, sensor size constraints, power consumption, and manufacturability, among others. By tailoring the microheater topology to align with the desired sensor performance characteristics, engineers and researchers can optimize the functionality of gas sensors for diverse applications and operational environments.

The careful design and optimization of microheater topologies are instrumental in tailoring sensor performance to specific application requirements, making them a critical component in advancing gas sensing technology. A power-compensated poly-Si microheater produced with the LPCVD process and with resistance control via phosphorous doping, using an ion implantation process, has been proposed in [14]. The uniformly heated area of the power-compensated microheater was approximately 2.5 times larger than that of the uncompensated microheater. In this scenario, the region where the temperature exceeded 90% of the maximum temperature encompassed over 80% of the total heating area. This points towards a considerable expansion of the heating area, demonstrating the suitability of the compensation design for the operation of a temperature-dependent semiconductor gas sensor. A small heating device is responsible for generating the necessary heat by passing a specific current through a resistor in [15]. These devices are utilized alongside metal oxide gas sensors to provide the required temperature to the film, which influences the sensor's sensitivity and selectivity. Additionally, they are employed to hasten the adsorption process between the sensitive layers and the gas species being detected. Micro-heaters have been produced from noble metals like platinum and gold because they offer the most favorable temperature range, accuracy, and stability. Various options for the topology of meander-type platinum heaters in chemical sensors fabricated on thin dielectric membranes using MEMS–silicon technology have been reported in [16]. Comprehensive studies have been conducted on the heater's current–voltage characteristics, with measure-

ments of heating rates at various currents. Experimental temperature characteristics have been obtained for various meander topologies, and heater options have been determined to ensure optimal heat transfer processes at a low power consumption of approximately 20–25 mW.

Meander-shaped microheaters feature a winding or zigzag pattern that allows for a compact layout within the sensor's design while providing efficient heat distribution across the gas-sensitive layer. This topology maximizes the heating surface area within a confined space, facilitating precise temperature control and uniform heat dissipation. The meander-shaped microheater topology is particularly well suited to applications where space constraints or specific geometric requirements are considered. Its versatile layout enables the integration of the heating element into diverse sensor configurations, contributing to enhanced thermal management and improved sensor performance. Exploring the integration of a meander-shaped microheater with a carbyne-enriched SAW gas sensor can offer unique perspectives on designing compact and integrated sensor platforms. Investigating the interplay between the exact microheater's layout, and sensor miniaturization can contribute to developing highly integrated and space-efficient gas sensing devices tailored to diverse application scenarios.

An investigation into carbyne-enriched surface acoustic wave (SAW) gas sensors with incorporated meander-shaped microheaters with different geometrical parameters is conducted for the first time, to the best of the authors' knowledge. This paper aims to explore the relationship between the heater geometry and the performance of SAW gas sensors with a carbyne-based sensitive layer. Understanding and optimizing the interaction between the heater design and the gas-sensitive layer is crucial for achieving a superior sensor performance. The integration of carbyne-enriched materials into SAW sensor technology and microheater technology represents a novel approach that has not been extensively explored in the existing literature. Moreover, the effect of the temperature on the carbyne-based sensor characteristics has not been thoroughly investigated in prior research. In this way, the work fills a crucial gap in the existing knowledge by exploring this unique combination for potential advancements in gas sensing applications.

## 2. Materials and Methods

Lithium niobate ( $\text{LiNbO}_3$ ) substrates were used to construct the SAW structures. This crystal is distinguished by the strong temperature stability of the coefficient of electromechanical coupling from 20 °C to 400 °C, and the changes in this coefficient, in this case, are 1.8% [17,18]. The substrates were cleaned in an ultrasonic bath with a solution consisting of isopropyl alcohol, acetone, and deionized water in a ratio of 1:1:3. Palladium thin film with a thickness of 280 nm was deposited via vacuum sputtering at an argon pressure of  $2 \times 10^{-2}$  Torr and sputtering voltage of 1.5 kV. Photolithographic patterning was conducted with a positive photoresist ma-P1215 (Micro resist technology) and wet chemical etching in heated mixture of nitric acid and hydrochloric acid (in a mixing ratio of 1:3). For the microheaters, reverse photolithography (lift-off) process was applied to avoid second chemical etching and reduce the quality of interdigitated (IDT) fingers of the SAW topology. A platinum film with a thickness of 280 nm was vacuum-sputtered on the backside of the substrates at  $2.10^{-2}$  Torr, and a sputtering voltage of 0.9 kV was grown over the photoresistive topologies, determined by three different geometrical parameters of the meander heaters (Figure 1a–c). The heaters were designed in COMSOL Multiphysics 5.4. (details in Supplementary Material—Figure S1a–d) with an appropriate width (in the range 300–450  $\mu\text{m}$  for the different topologies), length (1.2 mm for all samples), thickness (280 nm for all samples), and number of wires (1, 3 and 5), in order to provide maximal heating temperature of 80 °C, taking into account that the adsorbed organic analytes are volatile and greater temperature is not necessary.

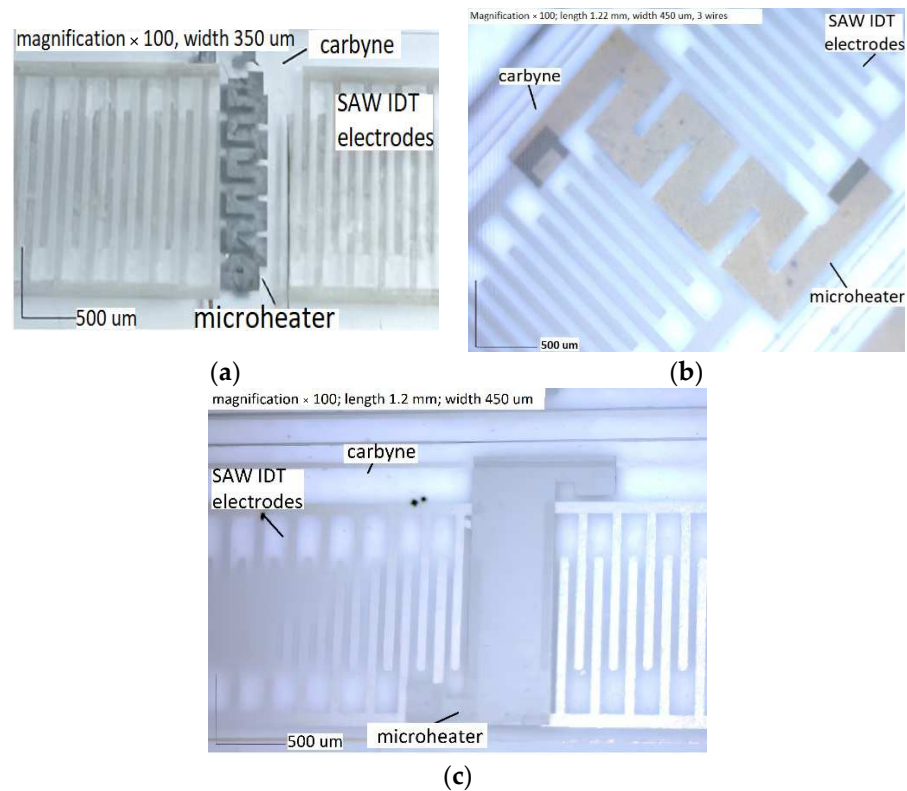


**Figure 1.** Images of the fabricated gas sensors with three different geometries of the microheaters: (a) small meander; (b) large meander; (c) dense rectangular.

Regarding the selection of the microheater contour shape, the following considerations were taken into account: for a spiral microheater, it is known from previous research that this configuration has a constant heating power per active area, which induces a hot spot in the heater center [19]. A spiral configuration, specifically the square one, consists of elongated straight tracks with numerous  $90^\circ$  turns. Previous studies have effectively showcased the capability to adjust the heating power within the active area by modifying the linewidth or the spacing or adjusting both the linewidth and spacing simultaneously [20], which is a complex approach. It has been proven that the spiral layout is only suitable for circular or square substrates. In contrast, for a rectangular substrate, a serpentine (or meander) heater is more compatible with the substrate's profile. Even for a square substrate, the modified serpentine heater can achieve a larger isothermal region than an optimized spiral heater [21]. Spiral microheaters can lead to greater lateral heat dispersion beyond the sensing area due to their radial nature. This heat diffusion could potentially interfere with the accuracy and efficiency of the sensing mechanism, leading to diminished sensor performance [22]. Managing and minimizing radial heat distribution is therefore crucial for maintaining the optimal performance and longevity of SAW gas sensor systems.

Afterwards, carbyne-enriched gas sensing film was deposited on the microheaters and the IDT electrodes via pulsed-plasma deposition through ion-assisted stimulation with specific energy levels. The distance between the target and the substrates was 1 m; the number of carbon plasma pulses was 3000; the voltage for an arc discharge ignited between the main discharge cathode holding the source of carbon and the main discharge anode holding the substrate was 300 V; the charge of the main capacitor that formed pulses of carbon plasma was  $2000 \mu\text{f}$  at 5 Hz; and the Ar-ion plasma power was 150 W. The thickness of the carbyne-enriched layer was 150 nm. Bonding was conducted with a semi-automatic ultrasonic wire bonder F&S Bondtec at conditions during packaging of the sensor device as follows: gold wire supplied via ball-wedge "stitch-ball" method (preliminary formation

of a ball for better stabilization and higher strength of the bond) at bond time of 50 ms, ultrasonic power of 50 W, bond force of 70 g, and substrate temperature of 100 °C.

Impedance of the samples vs. frequency for the three types of samples was measured using an impedance analyzer (Hioki IM3570, Ueda, Japan) in four terminal mode at a bias voltage of 1 V and frequency range 100 Hz–120 kHz (the accuracy for this frequency range is  $Z$ :  $\pm 0.08\%$ ;  $\theta$ :  $\pm 0.05^\circ$ ;  $C_s$ ,  $R_s$ :  $\pm 0.05\%$ ; see Figure 2a). The initial value for the sensor impedance before heating was 6.8 G $\Omega$  with a phase angle shift varying in the range of  $+209^\circ \div -213^\circ$ , the contact resistance of the electrodes was 4.6  $\Omega$ , and the interface capacitance between the electrodes and the gas-sensitive layer was 11.9 pF. The contact resistance and interface capacitance between the metal electrodes and carbyne-enriched detecting layer were monitored before and after desorption, activated with the different microheaters, to track initiation of local burnout due to potential irregular distribution of the thermal flow. The details for the functional testing of the SAW samples at different ethanol concentrations are described in our previous study [23] and shown in Figure 2b. In our previous study, it was found that a linear response in the sensor can be expected in the concentration range between 180 ppm and 680 ppm. The hysteresis curves for all microheater topologies were derived by exposing each sensor to increasing concentrations of the target vapor and measuring its response at each point. Afterwards, the microheater was activated for the desorption process, and the sensor exposure was repeated again to check to what degree its initial state was restored. The most informative parameter of the SAW sensor (time delay between the input and the output signal at a certain concentration) was tracked for change and expressed in percentage, aiming for the change to be as small as possible. The extracted information is new, because of the novel implemented carbyne-enriched material, highlighted theoretically as a perspective for sensing application, but still with insufficient practical implementation examples.

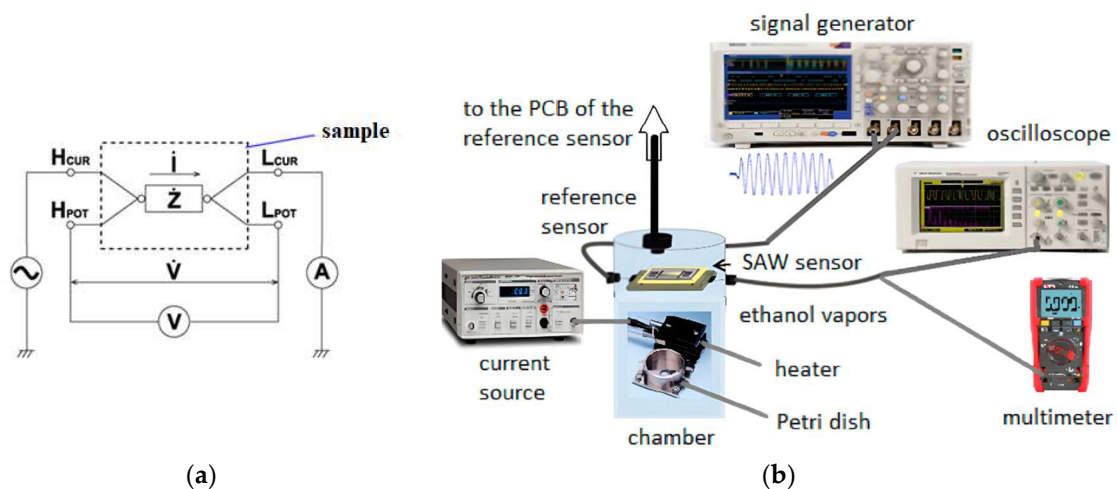


**Figure 2.** Test setup for the sensor samples: (a) measurement of the samples' impedance and contact parameters before and after heating; (b) measurement of the sensor's response characteristics at different ethanol concentrations [23].

### 3. Results

Before testing the sensor structure in heating mode, the piezoelectric properties of the LiNbO<sub>3</sub> substrate were evaluated in the temperature range from room temperature to the maximum heating temperature of 80 °C, provided by the heaters. Understanding the impact of temperature on the piezoelectric properties of the substrate is particularly important because it directly influences the sensor's sensitivity and response characteristics. The results are presented in Figure 3. It can be seen that at higher temperatures, the piezoelectric coefficient also increased. This is ascribed to the increased lattice spacing, which allows for greater freedom of movement for the charged particles within the crystal



lattice, thus resulting in an enhanced piezoelectric response [24]. Due to the high thermal stability of the LiNbO<sub>3</sub>, the contribution of this variation is with a factor of 0.12 for a temperature range of  $\Delta T = 55\text{ }^{\circ}\text{C}$ .

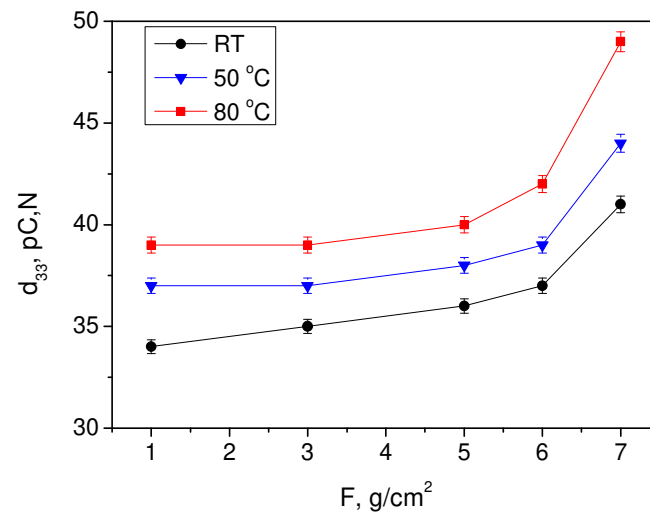


**Figure 3.** Piezoelectric properties of the LiNbO<sub>3</sub> substrate at different temperatures.

Figure 4a compares the contact resistance and interface capacitance formed between the carbyne-enriched sensing layer, the electrodes, and the substrate before ( $R_s$ ,  $C_s$ ) and after heating ( $R_{sh}$ ,  $C_{sh}$ ). As can be seen, the contact resistance deviates by approximately  $\pm 0.6\text{ M}\Omega$  from the average value of this quantity, no matter the delivered heat flow from any of the microheaters. Given the excellent thermal stability of the carbyne [25], this is expected behavior and can be interpreted as a lack of change in the sensing layer's microstructure. This is also supported by the change in the sensing layer resistance over the time graph for several hours exposed to the maximal temperature of the microheaters without analyte loading (Figure 4b), which is in the same range and close in values. The carbyne film resistance remains relatively constant over the 10 h duration exposed to the maximum temperature of the microheaters. The slight difference in the resistance can be ascribed to the thermal activation of defects, which are stimulated according to the power of the microheaters. Thus, the most powerful microheater (dense rectangular) activates deep and shallow traps, which, escaping the defect states, contribute to the conductivity of the film and reduce its overall resistance. On the contrary, the small meander activates only shallow traps, caused by impurities, due to its low power. Thus, the carbyne resistance, in this case, is almost unchanged compared to the film without heat exposure. Regarding the time dependence, it is visible that there is a trend for the initial release of the trapped charges during the first few hours. Afterwards, the resistances reach saturation and constant values are established. An exception can be noted for the small meander microheater, which is inert and needs more time to release even the small quantities of shallow traps. However, it can be noted that the interface capacitance increases gradually with the increase in the active area of the microheater—the lowest value of 6.5 pF was measured for the small meander, 8.65 pF was measured for the large meander, and the highest value of 12.5 was obtained for the dense rectangular shape, giving the fastest heating concentrated in the middle spot of the sensor between the two transducers. This behavior can be ascribed to thermally stimulated charges that were probably trapped in defect formations in the carbyne-enriched layer. These charges, together with the additional charges of the piezoelectric substrate produced after temperature increase (Figure 3), contribute to the higher capacitance. Therefore, the most prolonged time delay in the output signal is expected to be generated for the sensor with the dense rectangular microheater due to the time needed for the charge and discharge of the high-value capacitance.

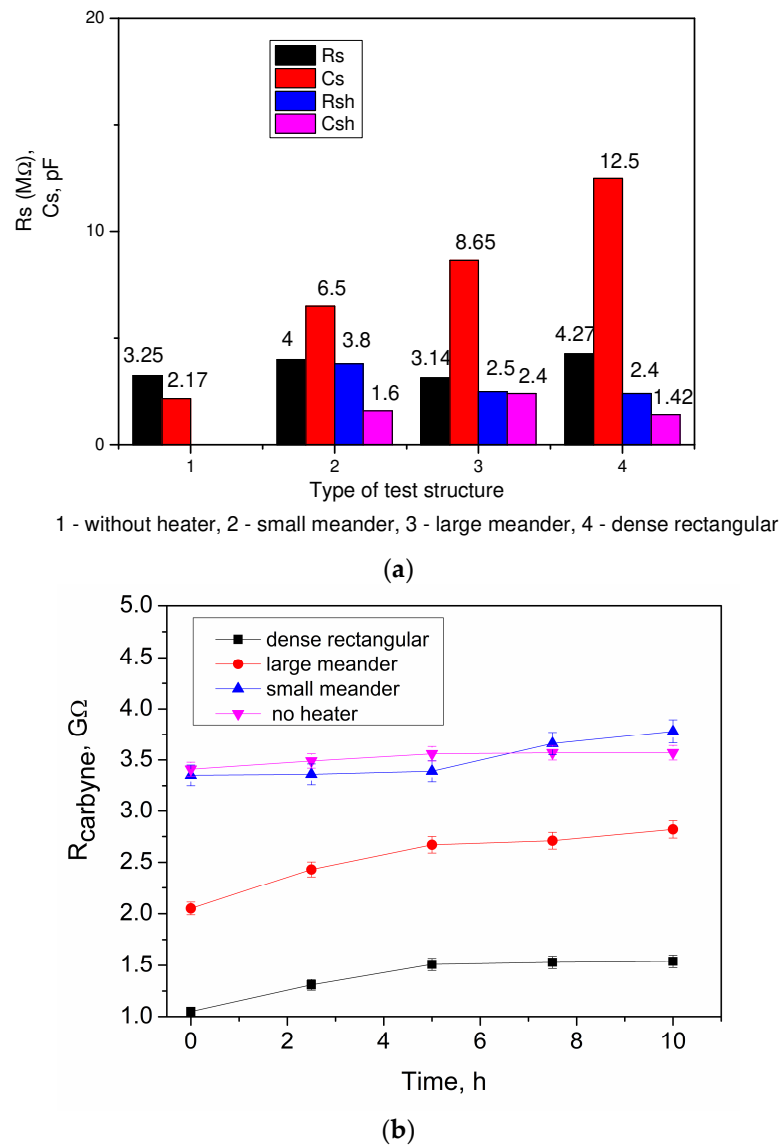


**Figure 4.** (a) Comparison of the contact resistance and interface capacitance changes before and after heating for the three microheaters topologies; (b) change in sensing layer resistance over time at different microheater topologies.

To explore the response characteristics of the sensors with the three microheaters topologies, their output voltage attenuation vs. input reference signal was measured and the time delay of the output electric signal referred to the input one was determined for two cases: the first detection of ethanol with concentration in the range of 180–680 ppm (before heater activation) and the next detections after the heaters were periodically switched on to desorb previously absorbed molecules. The curves related to the activated heaters are averaged from five consequent desorbing cycles. The difference between the separate measurements is less than 1%, which falls into the tolerance of the fabrication process accuracy.

Figure 5 shows the time delay and voltage attenuation of the sensor with the small meander microheater before (a) and after activating the heater (b). The attenuation of the output voltage  $\Delta V$  compared to the input reference signal was in the same range before and after the activation of the small meander microheater. Therefore, the meaningful quantity for the sensor recovering estimation can be the time delay  $\tau$  between the two signals. Figure 5 also shows the time delay and voltage attenuation of the sensor with the large meander microheater before (c) and after activating the heater (d). The maximum attenuation of the output voltage after desorption increased by approximately 100 mV,

which can be related to a change in the carbyne adsorption capacity due to the induced redistribution of the waves because of the broader thermal field spot, which can be related to alterations in the viscoelastic properties of the materials due to the broader thermal field spot. It could impact the acousto-electric transformation and lead to such a great change in the output voltage attenuation. Another possible explanation is that the altered thermal field may influence the adsorbate–surface interaction, potentially leading to enhanced adsorption or desorption kinetics and altering the acoustic properties of the surface [26]. Figure 5e,f show the time delay and voltage attenuation of the sensor with the dense rectangular microheater before and after activating the heater, respectively. The maximum attenuation of the output voltage after desorption increased by approximately 60 mV, and its absolute value is greater than for the two meander structures, which is related to the narrow dynamic range of the sensor.

Figure 6a shows the degree of recovery of the initial sensor state, or sensor hysteresis in the case of the small meander geometry of the microheater. The deviation of  $\tau$  from the initial value is 3.3% at the beginning of the measurement for low concentrations, 2.7% at the end of the measurement for high concentrations, and 2.3% in the range of 450–600 ppm (with no difference at 550 ppm), where the sensor response is linear, and its sensitivity is the greatest (the highest slope of the characteristic). The hysteresis is narrow, and it can be concluded that there is a satisfactory degree of recovery in the sensor properties after desorption, indicating the appropriate topology of the microheater and a proper technological flow that does not affect the other layers. The microheater successfully performs its function to cause the desorption of ethanol molecules without causing a local concentration of heat, which could induce defects in the crystal lattices of the materials and affect the sensitivity or dynamic range of the sensor. The power consumption of the microheater is 1.92 mW. Figure 6b shows the degree of recovery of the initial sensor state for the large meander microheater topology. It can be noted that the time delay is greater with two orders of magnitude longer than for the case of small meander. When the sensor is heated for desorption, the density of the gas-sensing layer is altered, leading to a modification in its interaction with the SAW. This altered interaction could result in a greater time delay as the SAW propagates through the piezoelectric substrate and the modified gas-sensing layer. This phenomenon can be ascribed to changes in the acoustic impedance or the velocity of the SAW due to the modified surface properties following the desorption cycle. The deviation of  $\tau$  from the initial value was 18.7% at the beginning of the measurement for low concentrations, 35.7% at the end of the measurement for high concentrations, and an average of 25% in the range of 450–600 ppm (with no crossing in the whole range), where the sensor response is linear. The hysteresis is broader than the small meander case, and it can be concluded that there is a weaker degree of recovery in the sensor properties after desorption. The broader hysteresis loop in the high concentration range and the consistent deviation from the initial value could indicate that the gas-sensing layer undergoes non-reversible changes, possibly affecting the interaction between the gas molecules and the sensor surface. These changes in the surface interaction could lead to the observed broadened hysteresis and the non-linearity in the sensor response at higher concentrations. This behavior could be linked to phenomena such as saturation effects or changes in the surface chemistry of the sensor, affecting its response characteristics, which require additional investigation. At higher concentrations, the broader hysteresis loop may indicate that the desorption and re-sorption processes lead to more significant and slow changes in the sensor's surface properties. This can result in a slower recovery to the initial state, causing a broader hysteresis loop in the output transducer's time delay compared to the input transducer. Conversely, at lower concentrations, the narrower hysteresis loop may suggest that the desorption and re-sorption processes have less impact on the sensor's surface properties, leading to a faster and more complete recovery to its initial state. Further studies on the specific surface processes and interactions occurring during desorption and sorption cycles would be needed to elucidate the underlying scientific mechanisms fully.



The power consumption of the large meander microheater is 4.63 mW due to the 2.5-fold higher resistance of the large meander compared to the small one.

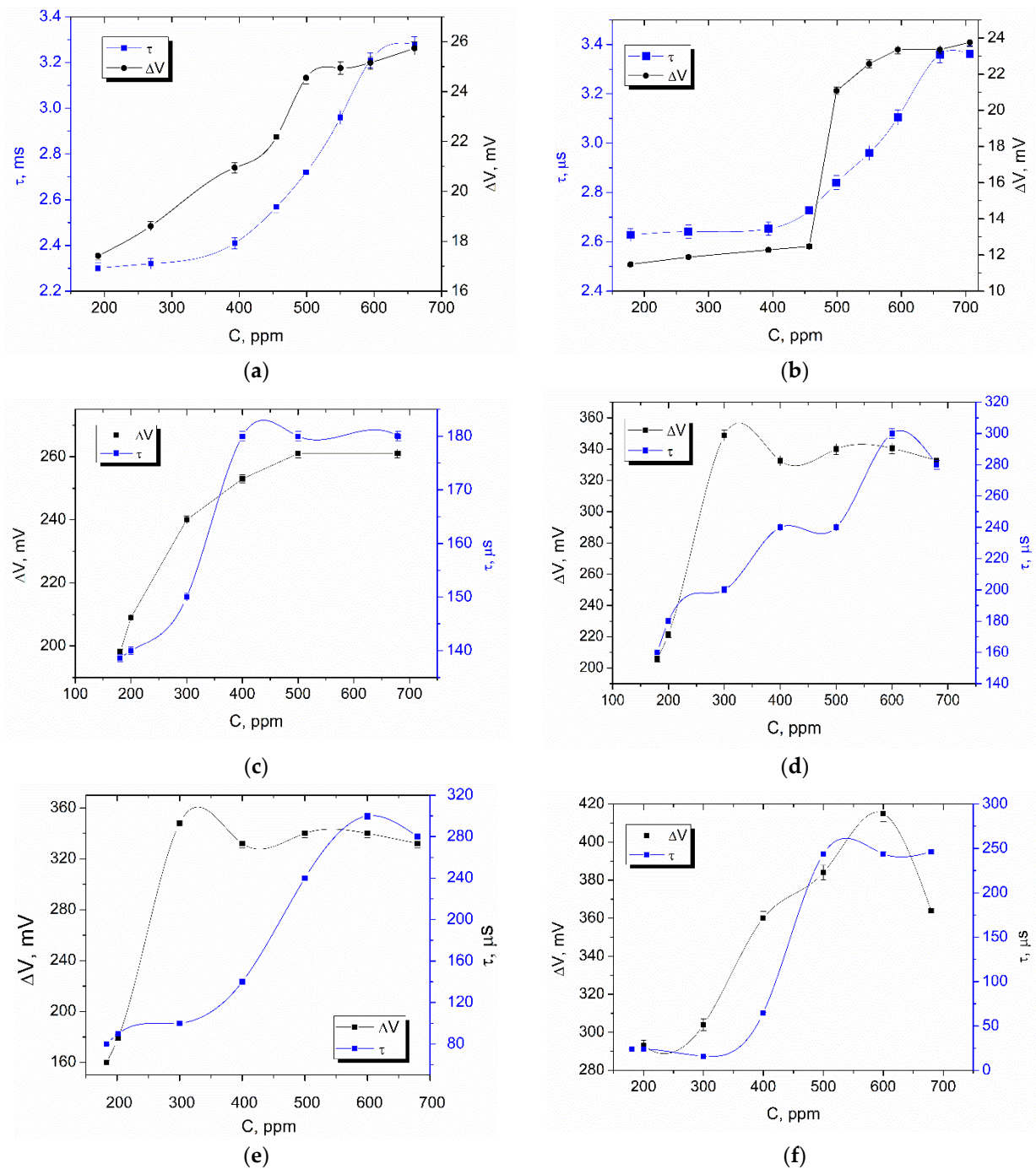


**Figure 5.** Time delay and voltage attenuation of the sensor with the small meander topology (a) before activating the heater, (b) after activating the heater (desorption). Time delay and voltage attenuation of the sensor with the large meander topology (c) before activating the heater, (d) after activating the heater (desorption). Time delay and voltage attenuation of the sensor with the dense rectangular topology (e) before activating the heater, (f) after activating the heater (desorption).

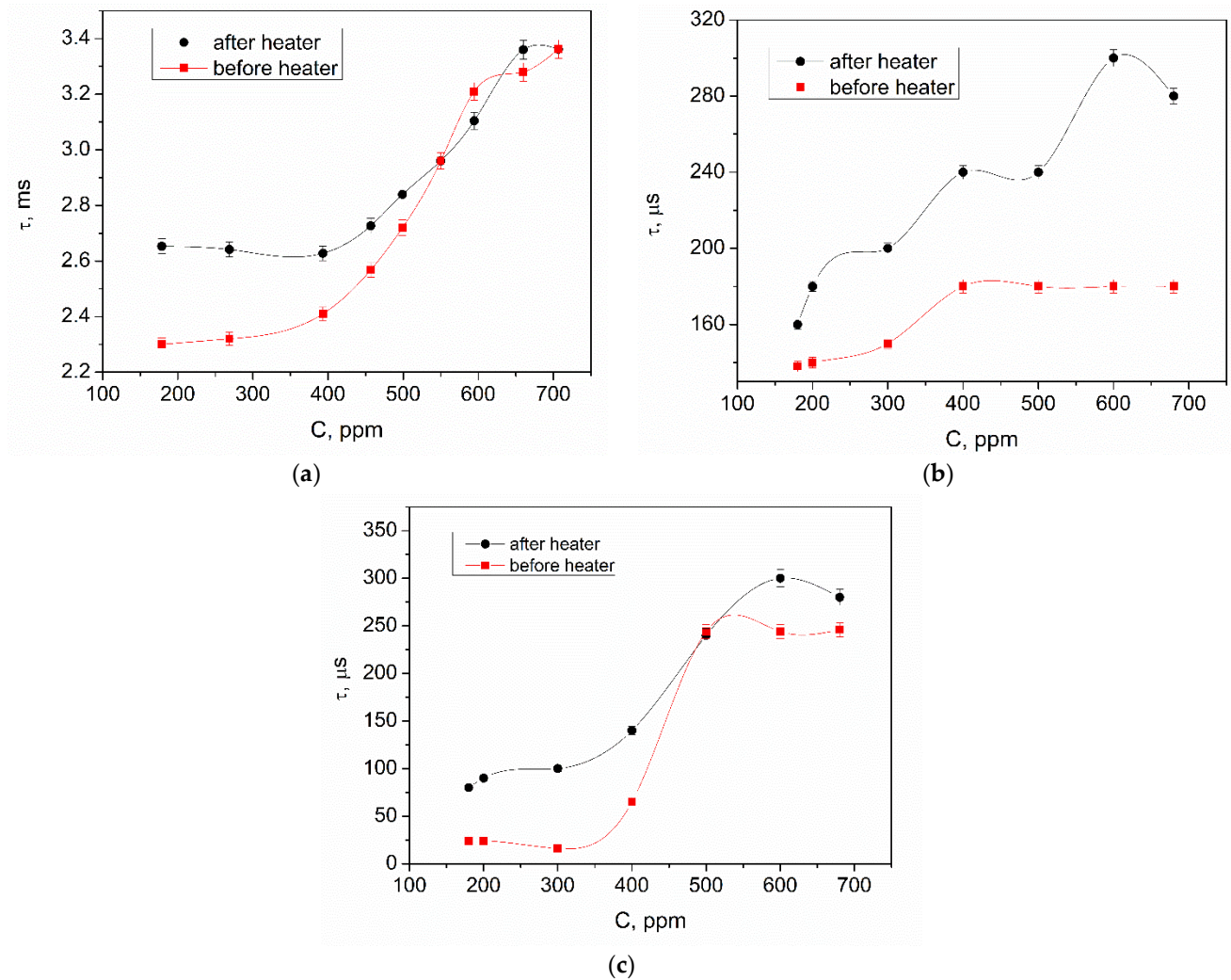


**Figure 6.** Hysteresis (recovery) of the sensor response (a) for the small meander microheater; (b) for the large meander microheater; (c) for the dense rectangular-shaped microheater.

For the dense rectangular topology, it can be noted that the time delay is the highest among all three types of microheaters (Figure 6c), but with the same order of magnitude as for the large meander. The deviation of  $\tau$  from the initial value is 30% at the beginning of the measurement for low concentrations, 12.1% at the end of the measurement for high concentrations, and an average of 26% in the range of 450–600 ppm (with crossing at 500 ppm), where the sensor response is linear. The hysteresis is broader than in the small meander case, but narrower in the range of high concentrations than in the large meander case. The desorption rate for the rectangular microheater is  $0.73 \mu\text{s/ppm}$  vs.  $0.33 \mu\text{s/ppm}$  for the large meander and  $0.03 \mu\text{s/ppm}$  for the small meander. The power consumption of the rectangular microheater is 10.65 mW due to the 4.8-fold higher resistance of the rectangular meander compared to the small one.

The basic sensors parameters and the effects of the microheater topology on them are summarized in Table 1.

Given the new information, the observed behavior between the accuracy and sensitivity of the sensors with different microheater designs suggests that the interaction between the microheater's heating pattern and the sensing element plays a critical role. The meander microheater likely provides a more uniform temperature distribution across the sensing area, contributing to a higher accuracy. In contrast, with localized heating, the spot high-density rectangular filled microheater results in a non-uniform temperature distribution, affecting the accuracy negatively. The meander microheater exhibits more con-

trolled and predictable heat transfer dynamics, leading to a more consistent and accurate response to changes in gas concentration. Meanwhile, the spot high-density rectangular filled microheater probably introduces unpredictable or non-linear heat transfer behavior, impacting the accuracy to a greater extent. The small meander-shaped microheater exhibits slower response times and reduced sensitivity to changes in temperature. Its thermal design delays the heating and cooling process, impacting the sensor's ability to detect rapid changes in gas concentration, which can be the reason for the lower sensitivity. It seems that the dense rectangular microheater positively affects the sensor's ability to accurately detect small fluctuations in gas concentration.

**Table 1.** Effect of the microheater topology on the sensor performance for the middle of the detecting range of ethanol vapors (430 ppm).

Microheater Topology	Voltage Sensitivity Change $\Delta S_v$ , %	Measurement Accuracy Change $\Delta \epsilon$ , %
Small meander	22 mV before heating 14 mV after heating $\Delta S_v = -36\%$	$\Delta \epsilon = 2.7\%$ (hysteresis 2.5%)
Large meander	330 mV before heating 255 mV after heating $\Delta S_v = -22\%$	$\Delta \epsilon = 25\%$ (hysteresis 23.3%)
Dense rectangular	370 mV before heating 330 mV after heating $\Delta S_v = -10.8\%$	$\Delta \epsilon = 21\%$ (hysteresis 19%)

Some results available in the literature related to the microheaters' parameters are summarized and presented in Table 2 for comparative purposes, considering the best results achieved in this work. In most of the studies, although the film for the microheater has similar properties (thickness, material composition) and operational temperature, the size of the microheater is larger and the design is more complex. As a result, the power consumption is also higher than that of the proposed structures at a similar hysteresis.

**Table 2.** Comparison of the basic parameters of gas sensor microheaters.

Microheater Geometry/Dimensions	Microheater Material and Thickness	Operational Temperature	Power Consumption	Transient Response	Sensor Hysteresis	Reference
Spiral/ 10 $\mu\text{m}$	PolySi/1 $\mu\text{m}$	300 °C	12.63 mW	11.5 ms	4.8%	[27]
Spiral square/ 1.5 mm $\times$ 1.5 mm	NiCr-Pt/10 $\mu\text{m}$	100 °C	6.5 mW	7 ms	3.4%	[28]
Meander/ 1 mm $\times$ 400 $\mu\text{m}$	PolySi-Au/500 nm	110 °C	N/A	N/A	2.9%	[15]
Interdigitated/ 1.2 mm $\times$ 1 mm	Invar/400 nm	100 °C	90 mW	N/A	N/A	[29]
Interdigitated/ 6 mm $\times$ 6 mm	Pt/200 nm	140 °C	N/A	N/A	10.3%	[30]
Small meander/ 1.2 mm $\times$ 300 $\mu\text{m}$	Pt/280 nm	80 °C	1.92 mW	0.33 ms	2.7%	This work

#### 4. Conclusions

Based on the results achieved, it can be concluded that the carbyne-enriched sensing layer, in conjunction with varying microheater topologies, demonstrates distinct behavior in response to the desorption and subsequent sorption of gas molecules. The investigation revealed that the contact resistance showed minimal deviation after heating, suggesting excellent thermal stability in the carbyne-enriched layer without any accompanying change



in microstructure. However, the interface capacitance did vary with the size and strength of the microheaters, potentially indicating the presence of thermally stimulated charges and additional charges from the piezoelectric substrate, resulting in higher capacitance. The analysis of sensors with different microheater topologies revealed distinct response characteristics. The small meander microheater presented efficient recovery properties, indicated by a low deviation in time delay at low and high concentrations, ultimately leading to a narrow hysteresis and linear sensor response. In contrast, the large meander and dense rectangular microheaters demonstrated a greater difference in time delay compared to the small meander with a broader hysteresis, potentially indicating non-reversible changes in the sensing structure. The significant increase in output voltage attenuation after desorption could be linked to alterations in the viscoelastic properties of the materials due to the broader thermal field spot. By considering the microheater topology factor, it is possible to gain a better understanding of why the meander-shaped microheater exhibits a loss of sensitivity, despite potentially providing other advantages, such as improved accuracy. This nuanced evaluation can guide further optimization efforts for the microheater design to achieve the desired balance between sensitivity and accuracy in the gas sensor system.

By analyzing the influence of the microheater's heating pattern on the sensor's response time, recovery kinetics, and repeatability of the sensing cycles, the investigation can provide novel insights into the dynamic behavior of carbyne-enriched SAW sensors with organic volatile compounds under varying exposure conditions. The variation in the microheater topology presents an avenue for optimizing the performance of the carbyne-based sensors, influencing their response characteristics toward organic vapors. Understanding the specific and detailed mechanisms underlying the interaction between the thermal field, the carbyne-enriched coating as a sensing material, and the desorption process require further investigation into the dynamics of heat distribution and their impact on desorption kinetics, which will be explored in our future work.

Our further research will be related to the further optimization of microheater parameters to reduce the measurement inaccuracy and avoid effects on the sensitivity of the sensors. Some error values can be ascribed to the direct connection of the microheater to the power supply without a control mechanism for the temperature and without compensation for the fluctuations in the supplied voltage and, as a consequence, the temperature. Therefore, a suitable control system for the microheaters will be built as a next step. Implementing advanced control algorithms to regulate the microheater's temperature can reduce fluctuations and enhance stability. In addition, implementing effective thermal insulation around the microheater can reduce heat loss and improve the heating rate, thereby enhancing the overall response time of the sensor.

**Supplementary Materials:** The following supporting information can be downloaded at: <https://www.mdpi.com/article/10.3390/app14051728/s1>.

**Author Contributions:** Conceptualization, M.A.; methodology, M.A. and G.K.; software, G.K.; validation, B.U.; formal analysis, M.A., I.R., A.T. and E.G.; investigation, M.A., T.T. and B.U.; resources, M.A.; software and simulations—T.T.; writing—original draft preparation, M.A.; writing—review and editing, A.T., I.R. and E.G.; visualization, M.A., B.U., T.T. and G.K.; supervision, M.A. and E.G.; project administration, M.A.; funding acquisition, M.A. All authors have read and agreed to the published version of the manuscript.

**Funding:** The research was funded by grant KP-06-DO02/2 CarbyneSense under ERA.NET RUS+ program, managed by BNSF. Some of the authors (IR, AT and EG) acknowledge the ERANET Project CarbyneSense MIS 5161208 for the financial support of this work.

**Institutional Review Board Statement:** Not applicable.

**Informed Consent Statement:** Not applicable.

**Data Availability Statement:** The data presented in this study are available on request from the corresponding author.

**Acknowledgments:** The authors are thankful to Alexander Lukin and Andrey Brigadin for their valuable help and providing the deposition of the carbyne-enriched material.

**Conflicts of Interest:** The authors declare no conflicts of interest.

## References

1. Hooshmand, S.; Kassanos, P.; Keshavarz, M.; Duru, P.; Kayalan, C.I.; Kale, İ.; Bayazit, M.K. Wearable Nano-Based Gas Sensors for Environmental Monitoring and Encountered Challenges in Optimization. *Sensors* **2023**, *23*, 8648. [\[CrossRef\]](#)
2. Márquez-Sánchez, S.; Huerta-Muñoz, J.; Herrera-Santos, J.; Arrieta, A.G.; De la Prieta, F. Gas sensing in industry. A case study: Train hangar. *Ad Hoc Netw.* **2023**, *148*, 103205. [\[CrossRef\]](#)
3. Chen, X.; Leishman, M.; Bagnall, D.; Nasiri, N. Nanostructured Gas Sensors: From Air Quality and Environmental Monitoring to Healthcare and Medical Applications. *Nanomaterials* **2021**, *11*, 1927. [\[CrossRef\]](#) [\[PubMed\]](#)
4. Sá, J.P.; Alvim-Ferraz, M.C.M.; Martins, F.G.; Sousa, S.I. Application of the low-cost sensing technology for indoor air quality monitoring: A review. *Environ. Technol. Innov.* **2022**, *28*, 102551. [\[CrossRef\]](#)
5. Laha, S.R.; Pattanayak, B.K.; Pattnaik, S. Advancement of Environmental Monitoring System Using IoT and Sensor: A Comprehensive Analysis. *AIMS Environ. Sci.* **2022**, *9*, 771–800. [\[CrossRef\]](#)
6. Pham, Y.L.; Beauchamp, J. Breath Biomarkers in Diagnostic Applications. *Molecules* **2021**, *26*, 5514. [\[CrossRef\]](#) [\[PubMed\]](#)
7. Javaid, M.; Haleem, A.; Singh, R.P.; Rab, S.; Suman, R. Exploring the potential of nanosensors: A brief overview. *Sens. Int.* **2021**, *2*, 100130. [\[CrossRef\]](#)
8. Gil, B.; Wales, D.; Tana, H.; Yeatmana, E. Detection of medically relevant volatile organic compounds with graphene field-effect transistors and separated by low-frequency spectral and time signatures. *Nanoscale* **2024**, *16*, 61–71. [\[CrossRef\]](#) [\[PubMed\]](#)
9. Lim, J.-B.; Reddeppa, M.; Nam, D.; Pasupuleti, K.S.; Bak, N.-H.; Kim, S.-G.; Cho, H.D.; Kim, M.-D. Surface acoustic device for high response NO<sub>2</sub> gas sensor using p-phenylenediamine-reduced graphene oxide nanocomposite coated on langasite. *Smart Mater. Struct.* **2021**, *30*, 095016. [\[CrossRef\]](#)
10. Mujahid, A.; Dickert, F.L. Surface Acoustic Wave (SAW) for Chemical Sensing Applications of Recognition Layers. *Sensors* **2017**, *17*, 2716. [\[CrossRef\]](#)
11. Luo, W.; Fu, Q.; Zhou, D.; Deng, J.; Liu, H.; Yan, G. A surface acoustic wave H<sub>2</sub>S gas sensor employing nanocrystalline SnO<sub>2</sub> thin film. *Sens. Act. B Chem.* **2013**, *176*, 746. [\[CrossRef\]](#)
12. Aleksandrova, M.; Kolev, G.; Brigadin, A.; Lukin, A. Gas-sensing properties of a carbyne-enriched nanocoating deposited onto surface acoustic wave composite substrates with various electrode topologies. *Crystals* **2022**, *12*, 501. [\[CrossRef\]](#)
13. Wu, Y.; Du, X.; Li, Y.; Tai, H.; Su, Y. Optimization of temperature uniformity of a serpentine thin film heater by a two-dimensional approach. *Microsyst. Technol.* **2019**, *25*, 69. [\[CrossRef\]](#)
14. Hwang, W.-J.; Shin, K.-S.; Roh, J.-H.; Lee, D.-S.; Choa, S.-H. Development of Micro-Heaters with Optimized Temperature Compensation Design for Gas Sensors. *Sensors* **2011**, *11*, 2580. [\[CrossRef\]](#) [\[PubMed\]](#)
15. Algamili, A.S.; Khir, M.H.; Ahmed, A.Y.; Rabih, A.A.; Ba-Hashwan, S.S.; Alabsi, S.S.; Al-Mahdi, O.L.; Isyaku, U.B.; Ahmed, M.G.; Junaid, M. Fabrication and Characterization of the Micro-Heater and Temperature Sensor for PolyMUMPs-Based MEMS Gas Sensor. *Micromachines* **2022**, *13*, 525. [\[CrossRef\]](#) [\[PubMed\]](#)
16. Gorokh, G.; Taratyn, I.; Fiadosenka, U.; Reutskaya, O.; Lozovenko, A. Heater Topology Influence on the Functional Characteristics of Thin-Film Gas Sensors Made by MEMS-Silicon Technology. *Chemosensors* **2023**, *11*, 443. [\[CrossRef\]](#)
17. Hauser, R.; Reindl, L.; Biniash, J. High-temperature stability of LiNbO<sub>3</sub> based SAW devices. In Proceedings of the IEEE Symposium on Ultrasonics, Honolulu, HI, USA, 5–8 October 2003.
18. Li, M.-H.; Chen, C.-Y.; Lu, R.; Yang, Y.; Wu, T.; Gong, S. Temperature Stability Analysis of Thin-Film Lithium Niobate SHO Plate Wave Resonators. *J. Microelectromech. Syst.* **2019**, *28*, 799. [\[CrossRef\]](#)
19. Miralles, V.; Huerre, A.; Malloggi, F.; Jullien, M.-C. A Review of Heating and Temperature Control in Microfluidic Systems: Techniques and Applications. *Diagnostics* **2013**, *3*, 33–67. [\[CrossRef\]](#) [\[PubMed\]](#)
20. Courbat, J.; Canonica, M.; Teyssieux, D.; Briand, D.; De Rooij, N.F. Design and fabrication of micro-hotplates made on a polyimide foil: Electrothermal simulation and characterization to achieve power consumption in the low mw range. *J. Micromech. Microeng.* **2010**, *21*, 196–201. [\[CrossRef\]](#)
21. Mele, L.; Rossi, T.; Riccio, M.; Iervolino, E.; Santagata, F.; Irace, A.; Breglio, G.; Creemer, J.F.; Sarro, P.M. Electro-thermal analysis of MEMS microhotplates for the optimization of temperature uniformity. *Proc. Eng.* **2011**, *25*, 387–390. [\[CrossRef\]](#)
22. Souhir, B.; Sami, G.; Hekmet, C.S.; Abdennaceur, K. Design, Simulation, and Optimization of a Meander Micro Hotplate for Gas Sensors. *Trans. Electr. Electron. Mater.* **2016**, *17*, 189–195. [\[CrossRef\]](#)
23. Aleksandrova, M.; Kolev, G.; Dobrikov, G.; Brigadin, A.; Lukin, A. Unlocking the Carbyne-Enriched Nanocoating Sensitivity to Volatile Organic Vapors with Plasma-Driven Deposition onto Bulk Micromachined Silicon Membranes. *Nanomaterials* **2022**, *12*, 2066. [\[CrossRef\]](#) [\[PubMed\]](#)
24. Dapeng, Z.; Qinghui, J.; Yingwei, L. The effect of temperature and loading frequency on the converse piezoelectric response of soft PZT ceramics. *Mater. Res. Express* **2017**, *4*, 125705. [\[CrossRef\]](#)
25. He, Y.; Xu, H.; Ouyang, G.; Yang, G. Thermal properties of carbyne nanostructures. *Results Phys.* **2022**, *34*, 105311. [\[CrossRef\]](#)



26. Taqui, S.N.; Syed, A.A.; Mubarak, N.M.; Farade, R.A.; Khan, M.A.M.; Kalam, A.; Dehghani, M.H.; Soudagar, M.E.M.; Rather, R.A.; Shamsuddin, S.Z.M.; et al. Insights into isotherms, kinetics, and thermodynamics of adsorption of acid blue 113 from an aqueous solution of nutraceutical industrial fennel seed spent. *Sci. Rep.* **2023**, *13*, 22665. [[CrossRef](#)]
27. Bhatt, P.; Arora, A. *Design of Microheater for MEMS Based Gas Sensor*; Thapar University: Patiala, India, 2014.
28. Kumar, V.V.; Sasikala, G. Design of Low Power Ni-chrome-Platinum Micro-Heater for MEMS-Based Gas Sensor in UAV Applications. *IJEEE* **2023**, *10*, 128–137.
29. Modal, S.S.; Roy, S.; Sarkar, C.K. Design and electrothermal analysis of MEMS based microheater array for gas sensor using INVAR alloy. In Proceedings of the 2012 International Conference on Communications, Devices and Intelligent Systems (CODIS), Kolkata, India, 28–29 December 2012; pp. 468–471.
30. He, L.; Wang, F.; Niu, G.; Gong, H.; Yang, Z.; He, W.; Cao, J. Design of Mems-Based Gas Sensor Micro Heat Plate. In Proceedings of the International Workshop on Materials, Chemistry and Engineering (IWMCE 2018), Xiamen, China, 16–17 June 2018; pp. 610–615.

**Disclaimer/Publisher’s Note:** The statements, opinions and data contained in all publications are solely those of the individual author(s) and contributor(s) and not of MDPI and/or the editor(s). MDPI and/or the editor(s) disclaim responsibility for any injury to people or property resulting from any ideas, methods, instructions or products referred to in the content.